Comparison of tropospheric correction techniques for two-pass DInSAR application in USCB region

Rafal Marciniak, *Student Member, IEEE,* Maya Ilieva, *Member, IEEE,* Karina Wilgan, *Member, IEEE,* Witold Rohm, *Member, IEEE,*

***Abstract*—The two-pass differential interferometric synthetic aperture radar (DInSAR) is a very useful tool for deformation monitoring. Although, to take full advantage of this technique, some sources of errors must be mitigated. Troposphere is one of the main sources of errors. If the tropospheric effect is not removed, it can be wrongly assumed as a deformation. In recent years, many methods of eliminating the tropospheric impact have been developed, some of them utilizing the external data sources.**

In this study, we compare several tropospheric correction models based on different methods and data sources: the Generic Atmospheric Correction Online Service (GACOS), the Collocation of Meteorological Data for Interpretation and Estimation of Tropospheric Path delays (COMEDIE), the Iterative Tropospheric Decomposition (ITD) model and the linear function model (LINEAR). The region of the presented research is Upper Silesian Coal Basin, a mining region in the South of Poland. This area is characterized by high mining activity, which results in highly non-linear large-scale deformations (1km^2). Testing the proposed methods of tropospheric corrections for this area defines their effectiveness on a local scale, as well as their impact on the interpretation of displacement maps.

The most effective methods for improving the displacements maps are: GACOS and COMEDIE models based on both Global Navigation satellite Systems (GNSS) and numerical weather prediction model. They all have an average improvement for all 17 considered interferograms of 2 mm. Although, the correction models for some of the dates have shown a degradation of the displacement maps. To evaluate the reasons for such behavior, we analyze a relation between the improvements and the weather conditions, especially water vapor, the most varying tropospheric parameter. The average correlation between the differential water vapor (dWV) from a SEVIRI radiometer on-board a MSG satellite and the improvement of the DInSAR maps is 0.71. We remove from the statistics some interferograms for which the correlation with the dWV is below 0.34. After the rejection of some cases, the average improvement for the best methods is at a level of 5 mm.

I. Introduction

OVER THE past three decades, the space-borne Synthetic Aperture Radar (SAR) interferometry (InSAR) has developed rapidly. Currently, it has many applications, from measuring of tectonic deformation to determining of the ice flow. The ability to observe these variable effects at large scales has made InSAR a suitable tool to detect effects of underground mine activity [1], especially for large areas. The launch of the Sentinel-1 satellites of the European Space Agency to the near-polar orbits in 2014, with simultaneous sharing of the collected data through the Copernicus program, has contributed to the improvement of detection processes and alerting about crustal movements.

The C-band radar on-board the Sentinel-1 satellites allows for the observations of the earth's surface, because this range of electromagnetic spectrum has the property of penetration through the atmosphere. The deformations based on InSAR technique are calculated using at least two images taken during two satellite passes. The atmospheric conditions during the repeat-pass usually differ from the first past. Thus, the atmosphere-induced errors are one of the main error sources for the differential InSAR (DInSAR). The fluctuations of the atmospheric delay may produce larger signal than the actual ground movement and increase other errors during processing, e.g. unwrapping process [2].

About 90% of the air mass is in the lowest 15 km of the atmosphere i.e. troposphere [3]. This part contains almost all water vapor, which is the most variable and difficult to model parameter [4][5][6][1][7]. The second component of the atmosphere that affects microwave radiation is the ionosphere [3]. Although, this study uses observations from the Sentinel-1 satellite in the C-Band frequency (5.6 GHz), for which the influence of the ionosphere is negligible [8].

In recent years, many methods of estimating the impact of the troposphere for the InSAR applications have been employed: using long time series of interferograms and so-called persistent scatterers (PS) [9], [10] or independent data sources, such as weather models [11], [12], Global Navigation Satellite System (GNSS) data [13], sounding data[14] and spectrometers or multispectral imaging [10]. Using the time series of the SAR data itself to remove troposphere effects does not require any external data sources and has high efficiency. A large number of scenes allows to specify the atmosphere phase window by studying the frequency trend of the atmospheric distortion [15]. However, the disadvantage of these technique is a requirement of a sufficiently large number of SAR images and stable long-term deformations. For the purpose of determining deformations in the shortest possible time, right after their occurrence, the possibility of using many interferograms is significantly limited. To calcu-

Manuscript received —- –, —-. This investigation is part of the realisation of the project EPOS-PL, European Plate Observing System, POIR.04.02.00-14-A003/16, funded by the Operational Programme Smart Growth 2014-2020, Priority IV: Increasing the research potential, Action 4.2: Development of modern research infrastructure of the science sector and co-fubded from European Regional Development Fund

The authors are with the Institute of Geodesy and Geoinformatics, Wroclaw University of Environmental and Life Sciences, 50-357 Wroclaw, Poland, (e-mail: rav.marcin.geodezja@gmail.com; witold.rohm@igig.up.wroc.pl; maya.ilieva@upwr.edu.pl).

Karina Wilgan is with Technische Universität Berlin, 10623 Germany (TUB) and GFZ German Research Centre for Geosciences, 14473 Potsdam, Germany (e-mail: karina.wilgan@gfz-potsdam.de).

late the deformations, using only two SAR acquisitions, the atmospheric corrections must be calculated using external data sources. A popular data source for tropospheric corrections are numerical weather prediction (NWP) models. The advantage is the coverage of possibly large areas (even global) and a reasonably high temporal resolution of usually 1 h. However, often the NWP models cannot detect local turbulent effects visible on the interferograms [4] due to their coarse spatial resolution and inability to model local events such as fog in highly varied relief [16]. Another external data source is the GNSS, which can provide the tropospheric delays with a very high time resolution (e.g. 5 min). The effectiveness of models based on GNSS data depends on the density and distribution of the stations [13]. A third possibility is acquiring the water vapor data from spectrometers and multispectral cameras of very high spatial resolution (<3 km). However, the spectrometers such as MODIS (NASA) and MERIS (ESA) have long time between acquisitions and they not penetrate fully the clouds [17]. Satellites such as MSG by EUMETSAT have no problem with time resolution, which is a result of their geostationary orbits, but the available spectral radiance images of water vapor are only for medium and high atmosphere [18].

The progressive automation of InSAR processing also requires an automation of tropospheric delay estimation. Currently available open-source services are: the Generic Atmospheric Correction Online Service (GACOS) [19], the Toolbox for Reducing Atmospheric InSAR Noise (TRAIN) [20] and the Python based Atmospheric Phase Screen Estimation (PyAPS) [21], which use different data sources and different estimation methods. In this study, we use the GACOS service, which employs the Iterative Tropospheric Decomposition (ITD) method based on the data from the high-resolution weather model (HRES) of European Centre for Medium-Range Weather Forecasts (ECMWF). We also utilize the ITD method for different data sources: ECMWF re-analysis model ERA5 and GNSS data. Another method is the least-squares collocation using software COllocation of MEteorological Data for Interpretation and Estimation of tropospheric (COMEDIE) developed at ETH Zurich [**?**], [**?**]. The inputs for this models are: data from the GNSS and Weather Research and Forecasting (WRF) model, which is computed at Wroclaw University [22]. Also, a simple linear model of calculating tropospheric delays as a function of the elevation is taken into consideration.

The presented models have already been subjects of many research, however, most of them focused on improving interferograms on a larger scale. The research area in this paper is the mining region of Upper Silesian Coal Basin (USCB) in the southern Poland. The size of this region is rather small, $\sim$5000 km^2, but at the same time it is densely populated, with 5 million inhabitants [23]. Intensive coal mining in this region, directly below the urban areas with a high level of infrastructure, causes a threat to human life and damage to infrastructure and buildings [24]. Correct and quick estimation of displacements is therefore a key to reduce the level of risk and one of the most advanced techniques that can be utilized for this goal is DInSAR. In this study, we are assessing the usability of the different tropospheric correction models for InSAR for such small region.

The use of models to improve the quality of DInSAR products, presented in many studies [17][25], determined their results on the basis of changes in statistical parameters for large data samples. This makes it possible to indicate whether the model is working properly or not. Despite the positive results of their implementation, there are cases where models did not work. Therefore, it should be demonstrated for which weather conditions and other parameters the given model can be used. In this study, we making this attempts by using the correlation coefficient of DInSAR products with phenomena that may affect them.

This introduction is followed by Section II introducing the location of the considered region, the SAR data and the auxiliary data used to build the correction models. Section III presents the methodology used to calculate the troposphere correction models. Section IV-B describes the methods to assess the improvement after using the correction models. Section V shows the results of using the proposed models and section VI discusses the possible shortcomings of the adopted methodology. Section VII summarizes the study.

II. Data

We assess the impact of different tropospheric correction models on selected interferograms taken in the Upper Silesian Coal Basin (USCB) region over the years 2017—2019. In this section, we describe the exact location of the aree, the SAR data, the meteorological conditions for each interferogram and the auxiliary data used for calculating the tropospheric corrections.

A. Location

The main source of electricity in Poland (approx. 46.4% in 2017) is burning of the coal. According to the forecasts by the Polish Ministry of Economy, the electricity consumption in Poland will increase by more than 9% by 2025 [26]. Most of the coal deposits (over 80%) are located in the USCB region, in the South of Poland. Figure 1 shows the location of the region. The red rectangle indicates the area covered by the interferograms which consists of 23% mining area. The region also includes densely populated Katowice urban area with around 2-3 million inhabitants. Active coal mining has been conducted there for about 200 years [24], resulting in deformations of the entire region from a few centimeters per year to a maximum of $\sim$0.5-1.0 m/year. The values of deformation at the actual mines locations are much higher (HOW MUCH?).

Figure 2 shows a closer view to the study area covering around 80 km x 60 km region. The USCB area is located mostly on highlands, which results in long periods of snowfall and frequent fog. Due to the snow cover, some parts of the region had to be removed from the SAR analysis based on the reports from the three meteorological stations located within the study area.

B. SAR data

In this study, we use the interferometric data from ESA's Sentinel-1 satellite. It is equipped with C-band radar with a

frequency of 5.6G Hz. The SAR acquisitions are taken from both ascending and descending track and for each of them the repeat-pass of the satellite is around 7 days.

We have analyzed the Sentinel-1 acquisitions from years 2017—2019 in order to select the dates for this study. The selection criterion was the ratio of coherent pixels for a particular interferogram to the number of coherent pixels over the whole study period. More information on the selection process can be found in [27]. Another criterion was the variation of water vapor (WV) values for the particular interferogram. The chosen dates exhibit large variability of WV, expressed as standard deviations of WV values over the entire area. The WV values are taken from Spinning Enhanced Visible and InfraRed Imager (SEVIRI) [18] on-board the EUMETSAT Meteosat Second Generation (MSG) satellite. Moreover, the availability of GNSS and NWP data was taken into account for the dates selection. Based on these criteria, 17 interferograms were selected for this study. Figure 3 shows the dates of all acquisitions with the selected 17 slave acquisitions. All the chosen acquisitions are in the ascending mode and the time is 16:32 UTC.

In SAR interferometry, it is common to choose one coherent point in order to reference all displacements to this point. In our case, a pixel in the center of the study area was chosen based on the level of the coherence as well as the distance from areas marked as weak scatters and surface stability (i.e. roads, buildings) [9]. Firstly, an area with expected stable points was selected. Then the pixels were extracted from each displacement and coherence map. On their basis, a point with the highest coherence coefficient [28] and the lowest variation in pixel value was selected.

C. Meteorological conditions

Defining weather conditions during the SAR imaging is crucial for the studying of troposphere delay models. It allows to separate the influence of the atmosphere on selected interferograms from the other source of error, such as seasonal snow cover on the ground. We extract the information about meteorological conditions directly from SYNOP stations using the OGIMET service[1]. The additional information about the WV content obtained from the radiometer SEVIRI in the medium infrared range (6.2μm) onboard the MSG satellite [29]. SEVIRI measures the radiated energy emitted from Earth of the entire image area in 12.5 minutes with ∼3 km spatial resolution and 15-minute intervals. Table I shows the meteorological reports including the WV mean values and their standard deviations, snow depth and general weather conditions for all the interferometric pairs. Please note that there are separate reports for master and slave acquisitions.

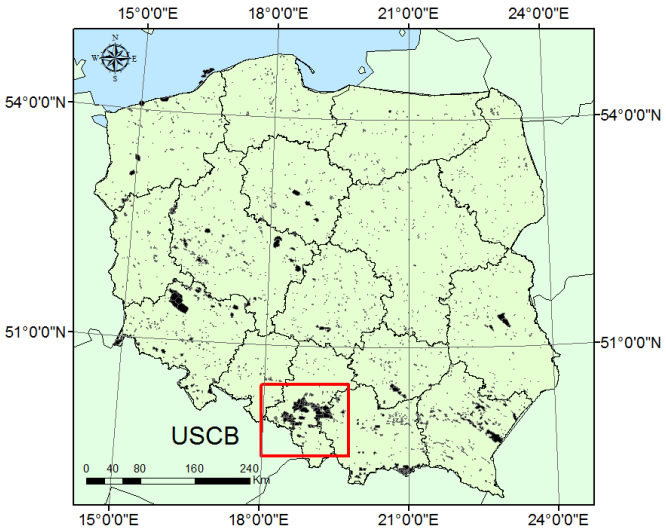

Fig. 1. The location of Upper Silesian Coal Basin region over the map of Poland. The red rectangle indicates the area of SAR acquisitions. The black polygons indicate the coal deposits.

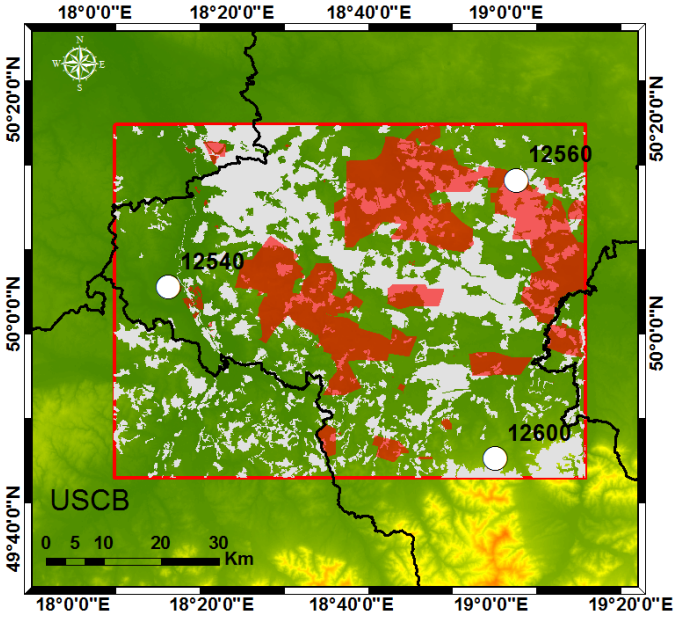

Fig. 2. The USCB area of the research (red rectangle). The mines are marked in red and the removed areas in gray. The meteorological stations are indicated by white circles

D. Auxiliary data

The troposphere correction models in this study are calculated from external data sources, namely GNSS and NWP data. Four of the models use GNSS data as an input and five of them use NWP models with different spatial resolution. The exact information on which data source is used in which correction model is provided in Tab. II. The GNSS data used for corrections is a part of the EUREF Permanent Network (EPN) as well as the stations installed by the Institute of Geodesy and Geoinformatics (IGIG) as a part of the EPOS project. There are from three up to eight stations located within the study area (Figure 2, ADD THIS!!). The resolution of the ZTD estimates is 0.5 – 1 h. The GNSS processing time (i.e. 30 minutes after full hour) is very close to the SAR imaging time (in a case of ascending track 16:32 UTC). The GNSS data allow also the detection of fast-changing events,

[1]www.ogimet.com

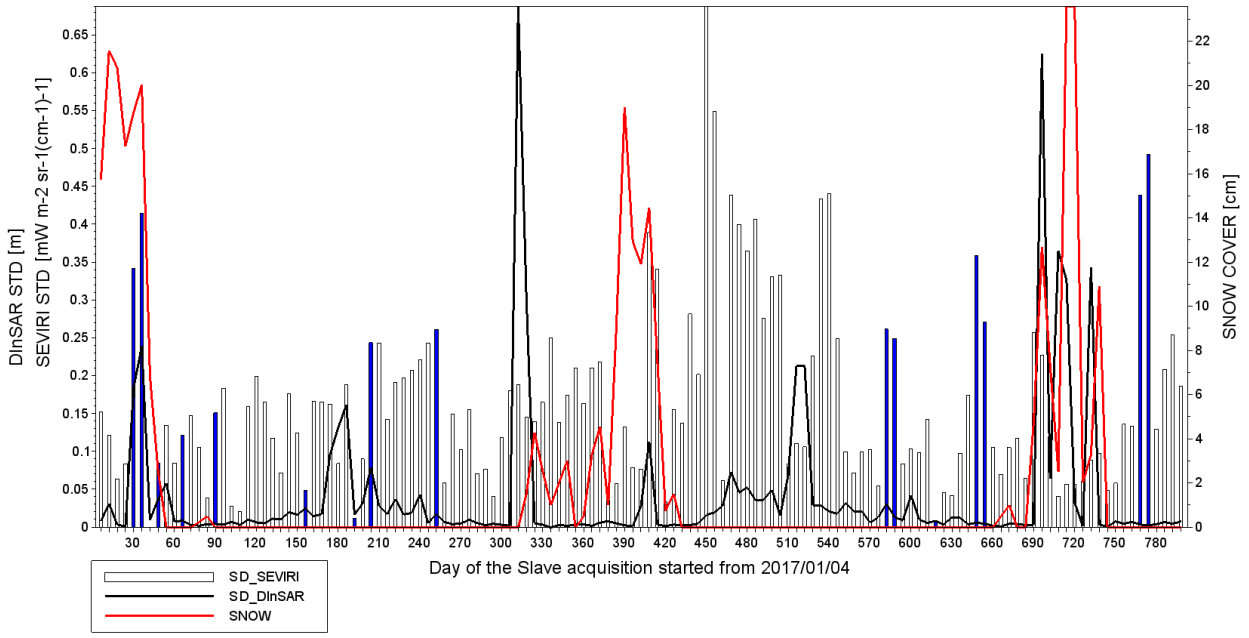

Fig. 3. All interferograms taken into the selection process. The bars indicate the standard deviations of water vapor values from SEVIRI satellite; the blue bars the selected dates; the black lines indicate the standard deviations of the displacement over the area and the red lines the snow cover averaged over three meteorological stations in the area.

TABLE I
WEATHER CONDITIONS DURING THE TIME OF ACQUISITION

Master	**Slave**	**Mean dWV**	**SD dWV**	**Snow dep.**	**Conditions – master acquisition**	**Conditions – slave acquisition**
DoY	[DoY]	[mW m^{-2} $(cm^{-1})^{-1}$]	[mW m^{-2} $(cm^{-1})^{-1}$]	[cm]	ST: 12560/12540/12600 SYNOP report for 15:00 UTC	ST: 12560/12540/12600 SYNOP report for 15:00 UTC
20170128	**20170203**	0.246	0.273	18.50	Haze/Mist/Haze	Fog/Mist/Fog
20170203	**20170209**	0.245	0.325	19.75	Fog/Mist/Fog	Overcast/Mist/Mist
20170209	**20170215**	-0.115	0.028	06.75	Overcast/Mist/Mist	Haze/-/Haze
20170215	**20170221**	0.205	0.089	02.50	Haze/-/Haze	Rain shower/Rain/Rain light
20170305	**20170311**	-0.773	0.115	00.40	Overcast/-/Overcast	Overcast/-/Overcast
20170329	**20170404**	1.095	0.136	00.00	Overcast/-/Broken	Broken/Broken/Overcast
20170609	**20170615**	0.417	0.063	00.00	Broken/Broken/Broken	Overcast/Broken/Broken
20170715	**20170721**	-0.326	0.036	00.00	Overcast/Overcast/Overcast	Overcast/Broken/Broken
20170727	**20170802**	0.092	0.203	00.00	Overcast/Overcast/Overcast	Rain shower/Broken/Broken
20170913	**20170919**	0.097	0.215	00.00	Overcast/Overcast/Overcast	Rain light/Rain light/Rain light
20180827	**20180902**	1.431	0.215	00.00	Broken/Broken/Broken	Overcast/Thunderstorm/Thunderstorm
20180902	**20180908**	-0.775	0.206	00.00	Overcast/Thunderstorm/Thunderstorm	Broken/Overcast/Mist
20181002	**20181008**	-0.088	0.034	00.00	Overcast/Overcast/Rain light	Broken/Broken/Broken
20181101	**20181107**	-0.465	0.285	00.00	Overcast/Overcast/Overcast	Overcast/Overcast/Broken
20181107	**20181113**	0.381	0.222	00.00	Overcast/Overcast/Broken	Overcast/Overcast/Overcast
20190313	**20190319**	-1.236	0.342	00.00	Overcast/Overcast/Overcast	Overcast/Overcast/Overcast
20190319	**20190325**	0.574	0.381	00.00	Overcast/Overcast/Overcast	Overcast/Rain shower/Overcast

such as thunderstorms, but only when the effects happen close to the antenna. The disadvantage of this source is the large dependence on the distribution and density of the GNSS stations. While moving away from the station, the ZTD prediction uncertainty increases significantly [13]. Since 2017, the network density has been constantly increasing, which is associated with a high demand for GNSS measurements in mining areas [30], as well as the availability of low-cost GNSS receivers as part of EPOS project.

We also use one medium-resolution and two high-resolution NWP models. The medium-resolution model is the European Centre for Medium Range Weather Forecasts (ECMWF) ERA5 atmospheric reanalysis [31]. The spatial resolution of ERA5 is 0.25°, which corresponds to 16 – 28 km at USCB latitude, with 37 vertical pressure levels. The time resolution of ERA5 is 1 h. Another model is the ECMWF high-resolution weather model (HRES) [32]. HRES provides the weather forecasts with a spatial resolution of 9 km and time resolution of 6 h. Second high-resolution model is the Weather Research and Forecasting (WRF) model provided by the Department of Climatology and Atmosphere Protection of the Wroclaw

TABLE II
MODELS USED WITH DATA SOURCES

Technique	Source	Spatial resolution	Temporal resolution
GACOS	HRES	∼8-14 km	6 h
ITD-GNSS	GNSS	<40 km	<0.5 h
ITD-GNSS/ERA5	GNSS/ERA5	<16 -28 km	<0.5 h+1 h
COMEDIE-WRF	WRF	∼4 km	1 h
COMEDIE-GNSS	GNSS	<40 km	<0.5 h
COMEDIE-GNSS/WRF	GNSS/WRF	<10 km	<0.5 h+1 h
LINEAR	ERA5	∼16-28 km	1 h

University [22]. It has a spatial resolution of 4 km with a temporal resolution of 1 h.

III. TROPOSPHERE CORRECTION MODELS

The tropospheric refractivity of the microwave signal can be divided into two parts: hydrostatic N_{hyd} and non-hydrostatic, often called as wet N_{wet} [3]. The total refractivity N_{tot} can be expressed as [3], [11]:

$$N_{tot} = N_{hyd} + N_{wet} = k_1 \frac{p}{T_v} + (k_2 - k_1 \frac{R_d}{R_v}) \frac{e}{T} + k_3 \frac{e}{T^2} \quad (1)$$

where p is air pressure, T is temperature, T_v is virtual temperature and e is water vapor partial pressure. Parameters R_d =287.05 Jkg^{-1}K^{-1} and R_v =461.495 Jkg^{-1}K^{-1} correspond to the gas constants of dry air and water vapor. k_1 =0.776 KPa^{-1}, k_2 =0.716 KPa^{-1} and k_3 =3.75$\times$10^{3}K^{2}Pa^{-1} are empirically refractivity determined coefficients.

The zenith total delay is then calculated as an integral of total refractivity [3]:

$$ZTD = 10^{-6} \int_{Z_0}^{Z_{Top}} N_{tot}(z) dz, \quad (2)$$

where Z_{Top} corresponds to the top layer of the troposphere. Next, the ZTDs are mapped into the slant tropospheric delay (STD) using a simple mapping function and converted into the interferometric phase ϕ_{tropo} along the line of sight (LOS) [17]:

$$\phi_{tropo} = \frac{-4\pi}{\lambda} STD == \frac{-4\pi}{\lambda} \frac{1}{cos(\theta)} ZTD(I_M), \quad (3)$$

where I_M is the chosen interpolation method, θ is the incident angle and λ is the wavelength of the microwave signal. Due to the repeat-pass imaging the path delay difference is equal to [13]:

$$\Delta\phi_{tropo} = \phi^M_{tropo} - \phi^S_{tropo}, \quad (4)$$

where M and S correspond to the master and slave image, respectively. Finally, the corrections are calculated relative to the chosen reference point REF:

$$\Delta\phi^{REF}_{tropo} = \Delta\phi_{tropo} - \Delta\phi_{tropoREF} \quad (5)$$

In this study, we use 7 models of tropospheric delay based on different input data sources and four interpolation methods. All of the models with their input spatial and temporal resolution are summarized in Table II. The four interpolation methods are described in this section.

A. *GACOS*

GACOS is an open-source package that generates ZTDs based on the HRES model [19]. To determine the dependence of the tropospheric correction with the terrain, a Shuttle Radar Topography Mission (SRTM) digital elevation model with a resolution of 90 m is used. The ZTDs in GACOS are separated into two components: turbulent and stratified, with an iterative decompose of the first [33], [25]:

$$ZTD_k = Tu(\mathbf{x_k}) + L_0 e^{-\beta \bar{h_k}} + \varepsilon_k \quad (6)$$

where Tu represent turbulent part of ZTD for the k-th location with x_k coordinates vector, ϵ are the un-modeled residual errors; the second term corresponds to the stratified component, which is represented by an exponential function of scaled height $\bar{h_k}$ for the k-th location and coefficients L_0 and β, which are estimated during the procedure. The coefficients are obtained by the ITD method, i.e. by gradually removing the turbulent part from the initial ZTD, assuming that in the first iteration $Tu(x_k) = 0$ and using the inverse distant weighting (IDW) method of interpolation. More details on the GACOS software can be found in [13], [25]. In [17], several correction methods were tested, i.e. GACOS, other weather models, GPS data and spectrometers for a case-study in the Unites States and Mexico. It was shown that GACOS reduced the most the displacement variation for distances over 75 km amongst all the tested methods. GACOS, as an external data source, allows for very fast estimation of tropospheric corrections for InSAR applications for long time series and different locations.

B. *ITD - Iterative Tropospheric Decomposition*

The ITD model, used in GACOS software, was also tested for other input data sources: GNSS and a combination of GNSS and NWP model ERA5. Adding the ERA5 data to the GNSS data should result in better estimation of the tropospheric conditions. We fit the ERA5 ZTDs to GNSS ZTDs locally from three to four closest stations assuming only linear dependence on the height [12]. The correction of k-th ZTD values for the ERA model is given by the equation:

$$\begin{aligned} v(E)_k &= ZTD(E)_k - (a_k H_k + b_k) \\ \wedge\ v(E)_k &\in [-|v(G)_k|_{max}, +|v(G)_k|_{max}] \end{aligned} \quad (7)$$

where E represents the ERA5 and G 3 closest GNSS ZTD values, v is the correction, H_k is the height of ERA5 k-th point and a_k and b_k are fitting function parameters.

The advantages of this method are: an increase in spatial resolution and a combination of lower to higher accuracy data through the use of weights and bias reduction. The disadvantage is a large dependence on the availability of data from the GNSS stations. Moreover, the data combination using the presented method is not error-free due to the influence of distant stations in the absence of data from nearby stations. This can be solved by setting some impact limit, in our case 150 km.

C. *COMEDIE*

Another interpolation method is the least-squares collocation using software COMEDIE developed at ETH Zurich [**?**],

[**?**], [**?**], [34]. In this method, each observation is divided into deterministic part (trend), a correlated stochastic (signal), and uncorrelated stochastic part (noise). The interpolated parameter is ZTD. The majority of the delay is determined as the trend part, while the variability and fluctuations are represented by the signal and noise. The equation of the deterministic part is expressed as:

$$ZTD(x,y,z,t) = [ZTD_0 + a(x-x_0) + b(y-y_0) + c(t-t_0)exp(-\frac{z-z_0}{H_0})] \quad (8)$$

where x_0 and y_0 are projected UTM coordinates, z_0 is orthometric height and t_0 is time of the reference point, and x, y, z, t correspond to the considered point. The results of solving the equation using the least-squares method are the estimated unknowns: ZTD_0, which is the ZTD at the reference position and time t_0, H_0: the scale height and the gradient parameters a, b, c in x, y and time, respectively. The stochastic correlated part is assumed to have normal distribution represented by a given covariance matrix C_{ss} depending on the 4-D distances of the points in the procedure. The stochastic uncorrelated part is also assumed to be Gaussian described by a covariance consisting of the noise of particular measurements on the diagonal. More details on the collocation technique can be found in [34]. In this study, we use three input data sources from which the ZTDs are calculated: GNSS, NWP model WRF and the combination of both. The advantages of collocation are: determining the variability of the phenomenon in time and space and dividing the delay into more than two components, which estimates fluctuations better. The disadvantage of the technique is being computationally demanding, which results in extended processing time.

D. *LINEAR*

The last method of estimating the path delay is simply modeling a linear dependence of the delay from the terrain height [12]. The parameters are computed using the least-squares method. The delay for each pixel is then calculated using the SRTM DEM. This method only takes into account the part of the delay related to the height of the terrain without any fluctuations or variability of the parameters. The ERA5 model is used as the data source. The ZTD for the k-th point is expressed as:

$$ZTD_k = a_1 H_k + a_2, \quad (9)$$

where H_k is the height of k-th point and a_1, a_2 are the linear parameters estimated in a least-squares sense.

IV. Verification methods

Different corrections strategies must be tested in order to find the best ones. At first, we compare all the tropospheric correction models to the reference GNSS data calculated directly at the stations locations. Moreover, we assess if the correction models remove the tropospheric impact for interferograms that should not have any deformations.

A. GNSS-based verification

The first validation of all models is carried out by comparing their values with data from the reference GNSS station. The root mean square of the differences is taken as a measure of the fit:

$$RMS = \sqrt{\frac{\sum_{k=1}^{n}(dZTD(I_M)_k - dZTD(GNSS)_k)^2}{n}} \quad (10)$$

where $dZTD(I_M)_k$ are the differential ZTDs for the chosen interpolation method I_M and k-th station; $dZTD(GNSS)_k$ are the $dZTDs$ at the k-th GNSS station location and n is the number of stations taken into consideration.

B. Assessment of the variability of deformations

The assessment of whether the DInSAR interferograms are corrected with different tropospheric models is not trivial, especially if we only use two images. The reason is that it is difficult to establish if certain structures presented in the images are an actual displacement or artefacts that need to be corrected. Moreover, in the USCB study area a long-term slow-slip deformation is observed [24], which has to be accounted for while using the correction models. Thus, in this study we focus only on interferograms taken within a short time interval. This allows to assume that only large-scale displacements (>10km) occur in the study area and no small-scale displacements (from ∼0.1 km to ∼1km) are observed. Based this assumption we determine using statistical parameters whether the image has improved or degraded. We quantify, if the standard deviations, biases (assuming that the expected value is 0) and a semi-variograms of the displacement has been changed after applying the correction models. The standard deviations of the displacement are calculated over the entire image area as:

$$\sigma_{\Delta\phi} = \sqrt{\frac{\sum_{i=1}^{m}(\Delta\phi_i - \bar{\Delta\phi})^2}{n-1}} \quad (11)$$

where m is the number of pixels, $\Delta\phi i$ are the relative phase values for i-th point and $\bar{\Delta\phi}$ is the average phase value from all the pixels. Then, the difference of standard deviations between uncorrected displacement $(\sigma_{\Delta\phi})_{DInSAR}$ and the displacement after using the corrections models $(\sigma_{\Delta\phi})_{DInSAR-MODEL}$ is given as:

$$\Delta\sigma_{\Delta\phi} = (\sigma_{\Delta\phi})_{DInSAR} - (\sigma_{\Delta\phi})_{DInSAR-MODEL} \quad (12)$$

The bias improvement is determined analogically, assuming that the expected value is 0:

$$Bias_{\Delta\phi} = \sqrt{\frac{\sum_{i=1}^{m}(\Delta\phi_i - \hat{0})^2}{n-1}} \quad (13)$$

$$\Delta Bias_{\Delta\phi} = (Bias_{\Delta\phi})_{DInSAR} - (Bias_{\Delta\phi})_{DInSAR-MODEL} \quad (14)$$

The third considered parameter is semi-variance estimating the improvement of the displacement maps on the dependency on the distance, which allows to evaluate the scale at which the

models are the most effective. The semi-variance is expressed as:

$$\gamma(r)_{\Delta\phi} = \frac{1}{2n}\sum_{i=1}^{n}[\Delta\phi(x)_i - \Delta\phi(x+r)_i]^2 \qquad (15)$$

where x is the location of i-th pixel and $x+r$ is the location of a pixel located at the distance r from the i-th pixel. The difference of the semi-variogram between the uncorrected and corrected images is then given as

$$\begin{aligned}\Delta\gamma(r)_{\Delta\phi} = (\gamma(r)_{\Delta\phi})_{DInSAR} \\ -(\gamma(r)_{\Delta\phi})_{DInSAR-MODEL}\end{aligned} \qquad (16)$$

These differences are dependent on the distance r between the pixels.

V. Results

We have calculated the tropospheric correction models based on seven correction scenarios (different methods and data sources) for 17 interferograms in the USBC region. In this section we validate our models, find the similarities between them and assess if and when they can be useful for DInSAR technique. Moreover, we try to relate the improvement/degradation of the interferograms with the water vapor conditions from the SEVIRI satellite data.

A. Correlations between the models

At first, we take a look at the similarities between models. Tab. III shows the correlation values between all considered models. It shows that the largest correlation (R=0.993) is between the COMEDIE-mix and COMEDIE-WRF. The COMEDIE-mix model is mostly based on WRF data, as many of the GNSS observations are rejected in the process as outliers. The COMEDIE-GNSS model is not so highly correlated with the other two COMEDIE-based models, with the correlation factor only slightly exceeding 0.5. Although, there is a high correlation between the two models employing the GNSS data: COMEDIE-GNSS and ITD-GNSS (R=0.722). Also, GACOS and the GNSS-based data has a correlation coefficient higher than 0.5. The worst correlation with all other models is represented by the LINEAR model and ITD-mix (both using ERA5 as the input data source).

B. Validation with the GNSS data

We compare the ZTDs from the correction models with the values calculated directly at GNSS stations in the area of interest. We calculate the RMS values for each model according to Eq. 10. Figure 4 shows the the RMS values for all 7 correction strategies. The highest RMS values are obtained for GACOS model with the RMS of 17.2 mm averaged from all interferograms and ITD-GNSS with the average of 29.4 mm. The value for GACOS is not very surprising, as this model does not use GNSS data at all. Although, the high value for ITD-GNSS can only be explained by the fact that this method is not so well applicable for turbulent effects in low density networks. On the other hand, the ITD-mix model exhibits the smallest error, which can be related to the fact that we attribute very small errors for GNSS data in this model compared to the errors from ERA5 model. The COMEDIE-based models, both from GNSS and WRF data have also a very good agreement with the reference GNSS data.

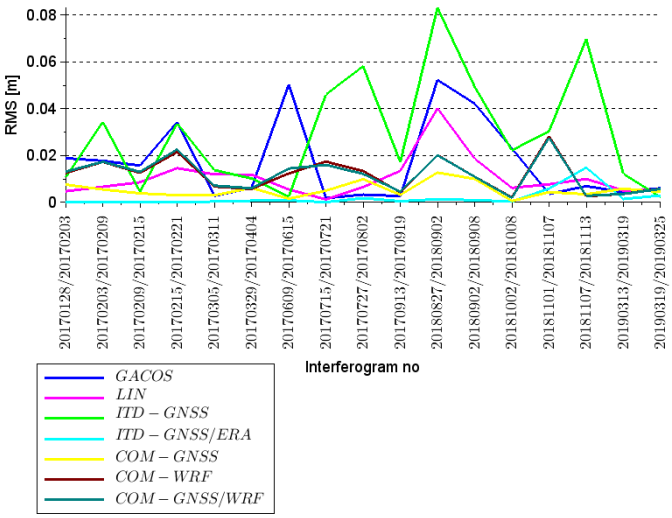

Fig. 4. The RMS values for each model compared to the reference GNSS data.

C. Deformation assessment

The main validation of the correction models is applying them for the selected 17 interferograms and the assessment of the deformation statistics as described in section IV-B. We compare the standard deviations, biases and semi-variograms of the interferograms before and after applying the correction models and assess whether there has been an improvement or degradation in the statistics using the proposed models. Figure 5 shows the improvement in standard deviations after using the correction models.

Based on the standard deviations improvement, shown in Fig. 5, the results are very diverse. For the first two interferograms, most of the methods shows improvement, with the largest one (∼1-2 cm) being for COMEDIE-based models. Unfortunately, there are also interferograms for which there is a degradation after using the proposed correction models, with the worst degradation of more than 1 cm for ITD-GNSS model for the 16th interferogram. For most of the dates, there is a mixture of improvement and degradation, depending on the model. These results show the necessity to indicate for which tropospheric conditions the models are most suitable for. Another factor that contributes to the level of improvement is the number of GNSS stations taken into account for the GNSS-based models. An interesting observation is that for the last three interferograms, the degradation was the largest, but at the same time, the number of used GNSS-stations in the area increased from three to eight. The worst results from all models shows the ITD-GNSS, presenting twice larger degradation for the case of 20190313-20190319 than the other models. Logically, adding more stations to the solution, should improve it, but these stations were installed in a very small area compared to the study area. Thus, it is possible that a

TABLE III
THE CORRELATION COEFFICIENT BETWEEN EACH MODEL.

	GACOS	LINEAR	ITD-GNSS	ITD-mix	COM-GNSS	COM-WRF	COM-mix
GACOS	1	-	-	-	-	-	-
LINEAR	0.187+/-0.104	1	-	-	-	-	-
ITD-GNSS	0.468+/-0.122	-0.046+/-0.106	1	-	-	-	-
ITD-mix	0.036+/-0.078	-0.036+/-0.053	0.081+/-0.102	1	-	-	-
COM-GNSS	0.565+/-0.103	0.165+/-0.110	0.722+/-0.098	0.106+/-0.095	1	-	-
COM-WRF	0.438+/-0.154	0.182+/-0.122	0.474+/-0.151	-0.052+/-0.071	0.510+/-0.150	1	-
COM-mix	0.446+/-0.154	0.183+/-0.122	0.481+/-0.151	-0.034+/-0.072	0.518+/-0.146	0.993+/-0.004	1

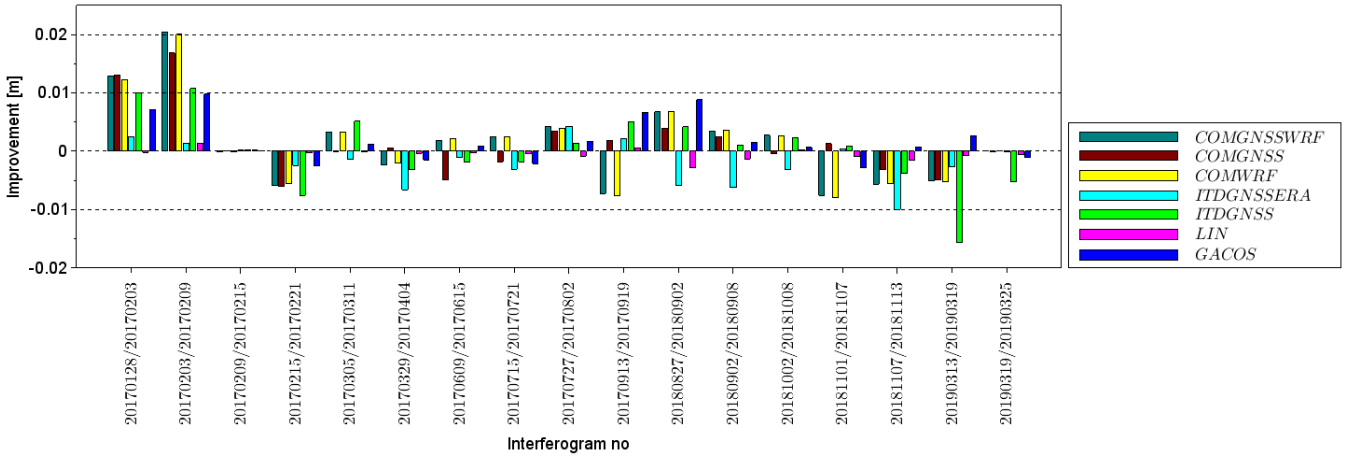

Fig. 5. Improvement of the standard deviations for the displacement for each interferogram.

network of stations with a more uniform distribution should solve this problem.

Figure 6 shows the average improvement for each model. The highest value of ∼2 mm is for GACOS and COMEDIE-based models. There are two models, for which there is a degradation on average: LINEAR and ITD-mix. The LINEAR model only depends on the relation between the delay and the heights and hence, the correction introduced by this model has a very small value and a very small variation. On the other hand, the ITD-mix model has on average introduced a degradation, but this model has a large variation for results, thus, for some of the dates it also yields improvement. At the same time the ITD-GNSS model presents better results. Thus, adding the ERA5 data deteriorates the model, which may be a result of the low spatial resolution of the weather model or the data itself.

Considering the improvement in the bias shows similar results as for standard deviations. The only difference is the increase of the mean improvement for the ITD-GNSS model by ∼1mm. The semi-variance is another important parameter to consider, because it associates the magnitude of the improvement with the size of the implemented structures (i.e. the distance between the pixels). Figure 7 shows an improvement of the displacement maps for each correction

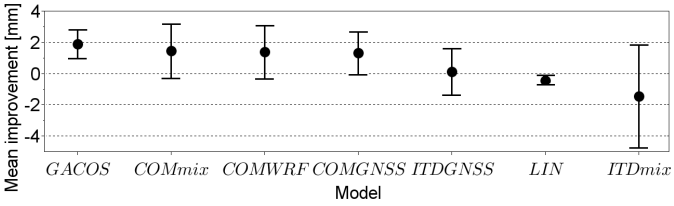

Fig. 6. The mean improvement of standard deviations for each model averaged over all interferograms.

model.

In general, all the correction models shown in Fig. 7 follow the same improvement pattern, which increases with increasing distance. Below ∼20 km there is almost no difference between the models. The improvement increases faster for distances larger than ∼40 km, mainly due to the influence of large atmospheric phenomena structures on SAR images and their modeling. The best models are the ones based on GNSS, i.e. COMEDIE-GNSS and ITD-GNSS and also GACOS. The worst ones are as in the case of previous statistics, LINEAR and ITD-mix models. However, the variability of the improvement, expressed in 1σ value is quite large, which does not allow us to fully state the suitability of the models used.

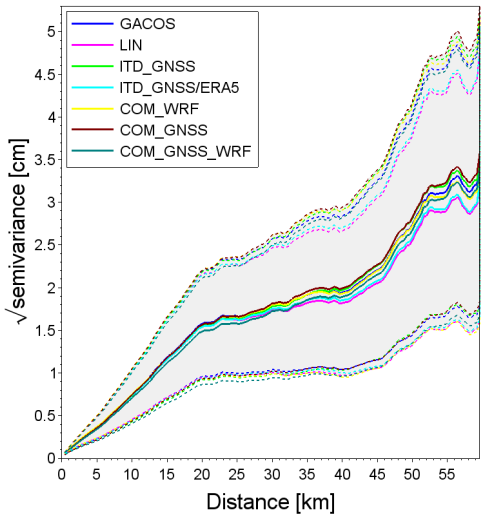

Fig. 7. Mean improvement for semi-variance averaged from all interferograms. The dashed lines correspond to 1σ for all cases. The positive values indicate improvement, while negative (not present) degradation.

The lack of significance for improving semi-variance is in agreement with the Murray et al study [17], where the semi-variance showed no significant improvement below ∼75km. Considering individual dates, there is large discrepancy in the range of improvement. Fig. 8 shows the semi-variance for one interferogram: 20181107-20181113. In this case, similarly to the above-mentioned standard deviations, there is a degradation visible for all models. It shows, that the same models for individual interferograms can show very different results. Thus, there is a need to determine in which conditions our correction models can be used.

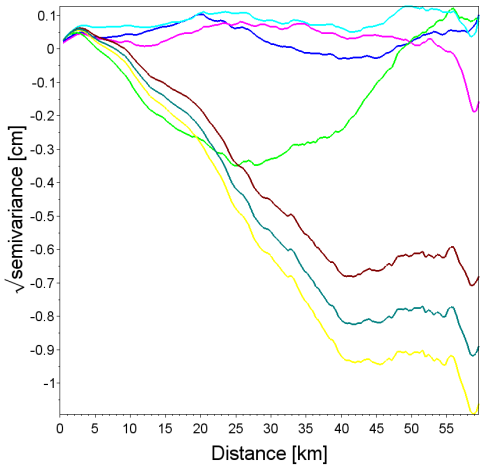

Fig. 8. Improvement in semi-variance for case 20181107-20181113. This semi-variogram shows degradation.

D. Comparisons with SEVIRI WV maps

To assess if the weather conditions have an impact on the improvement for different correction models, we compare them with the satellite water vapor data from EUMETSAT MSG satellite. The differential water vapor (dWV) values are calculated using spectral radiance imaging of the SEVIRI radiometer.We check the correlation between the dWV maps from SEVIRI and the DInSAR displacement improvement values based on the standard deviations improvement. Fig. 9 shows such correlation for each of the correction models. We show only one plot for COMEDIE-mix and COMEDIE-WRF model as we have shown in section V-A that these models are nearly identical.

As shown in Fig. 9, the correlation between the dWV values and the improvement averaged from all models is moderately high (R=0.71±0.075). The correction models with the highest correlation are: GACOS and two GNSS-based models: COMEDIE-GNSS and ITD-GNSS. As usual, the ITD-mix and the LINEAR models show low correlation. The fact that the correlation is low for the LINEAR model, confirms the earlier assumption that the consideration of water vapor distribution has an effect on tropospheric correction models.

The correlation coefficient for the COMEDIE-WRF model equals to 0.445 ± 0.143. The low correlation, compared to the COMEDIE-GNSS model, is affected mostly by one interferogram: 20170913-20170919. After removing this case, the correlation coefficient increases to 0.653 ± 0.093. We check the correlation coefficient for each correction model and interferogram. For the interferograms that showed degradation, the correlation between dWV and DInSAR images is below 0.34. For R>0.34, there is an improvement after using the proposed correction model. For R>0.56, the improvement is larger than 2 mm. We remove from the general statistics the interferograms for which the correlation coefficient is smaller than 0.34. Out of 17 cases, 9 cases were rejected and 8 were left. Figure 10 shows the mean improvement in standard deviations values and Fig. 11 shows the improvement in semi-variation for each model after removing the cases of low correlation.

As shown in Fig. 10, after rejecting the cases for which the correlation with SEVIRI dWV was too low, the average improvement for most of the correction models has been increased. Five models, that previously (shown in Fig. 6) has an average improvement of ∼2mm, now have an improvement at a level of ∼5mm. The largest improvement after rejecting some cases is for the ITD-GNSS model, which previously showed an almost-zero improvement, while now the improvement for this model is on the level of 4 mm. The LINEAR model remains unchanged and the ITD-mix model still shows a small average degradation with the large spread of values. For semi-variance, shown in Fig. 11, the increase in improvement after rejecting some cases is also visible in the semi-variance. The improvement in semi-variance compared to Fig. 7 increases by ∼1 cm for the distance of 20 km, by ∼2 cm for the distance of 40 km and by ∼3 cm for the distance of 60 km. However, it the rejection of some cases does not reduce the uncertainty of the semi-variogram result, which is still at the same level as before.

VI. Discussion

The tropospheric correction models for InSAR applications has been very popular over the past years [20], [19], [21].

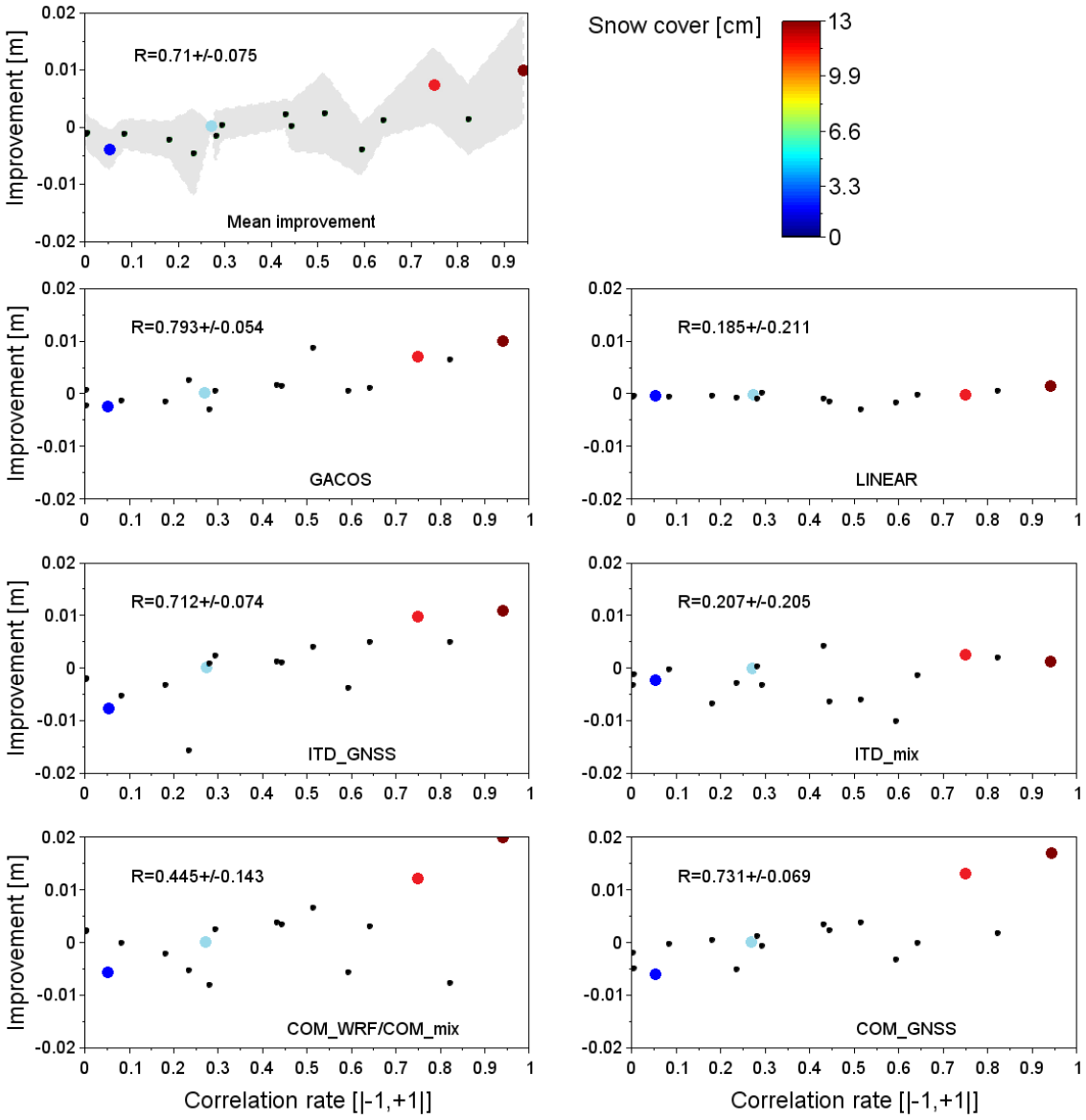

Fig. 9. Correlation between the dWV values from SEVIRI and the improvement of the displacement maps in terms of standard deviations. The color dots represent the days with snow cover. The shaded area for the top picture (averaged improvement from all methods) represent 3σ value.

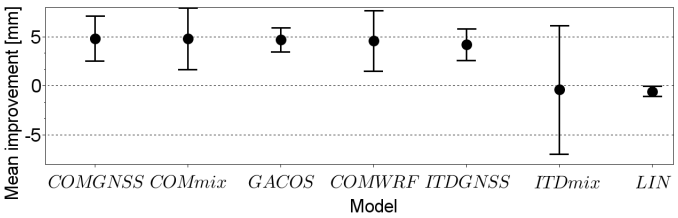

Fig. 10. The average improvement of the standard deviations of the displacement maps for each model after rejecting the cases with low correlation with dWV.

Different correction models have been tested and their effectiveness in reducing the tropospheric impact on the interferograms was proven [25], [11], [14]. Although, for many cases, the models were calculated for large areas (>100km). Atmospheric structures at such scale are easily detectable by weather models, GNSS stations or other techniques[17]. However, in this study, we consider only a very small area with local atmospheric conditions. Unfortunately, the implementation of the correction models for small-scale phenomena does not provide such positive results as for large-scale. Despite the average statistical reduction of variance (Fig. 6), for many cases the degradation of the DInSAR displacements could be found due to the increased role of turbulent effects for such scale. These effects are very difficult to be detected by the weather models, or other techniques, which can define the state of the atmosphere [3], due to:

1) spatial resolution of those effects,
2) high variability in time,
3) high variability in space (horizontally and vertically).

The main factor associated with this phenomenon is water

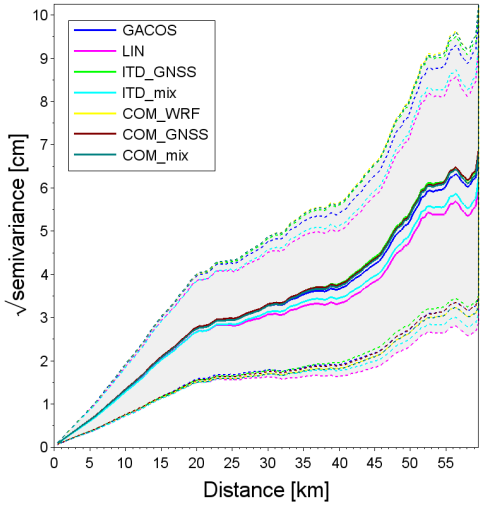

Fig. 11. The improvement for the semi-variance after rejecting the cases with low correlation with dWV. The shaded area corresponds to 1σ value

vapor [4], [5], [6], [1], [7]. Thus, the effective modeling of the water vapor content in the troposphere is a key factor of obtaining the right tropospheric corrections for DInSAR. In this study, we show that a correlation between the improvement of the displacement maps and water vapor content exists (Fig. 9). We rejected some of the interferograms based on the correlation coefficient of the dWV maps and the improvement. In total, 9 out of 17 dates are rejected. Figure 12 shows the improvements in semi-variance before and after rejecting the cases for which the correlation of the water vapor maps is too low. The average improvement after the rejection is very clear.

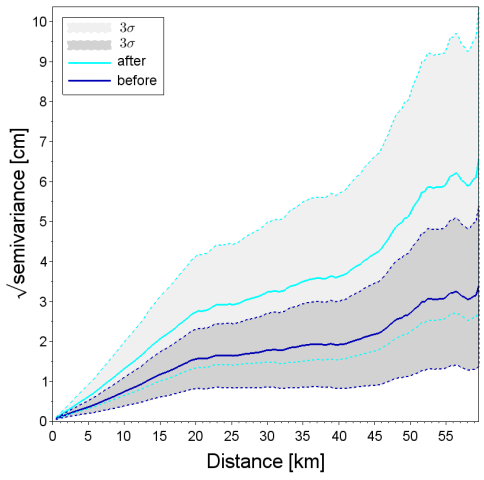

Fig. 12. Improvement of the quality in semi-variance before (dark blue) and after (cyan) rejecting cases for which the correlation with SEVIRI dWV was too small. Shaded area correspond to 3σ value.

The rejected cases mostly shows degradation of the variance parameters after applying the tropospheric corrections models. However, for two of the interferograms, the COMEDIE-WRF model actually show an improvement in terms of standard deviations: of -2.2 mm for the case 20170609-20170615 and -2.5 mm for 20170715-20170721. The COMEDIE-WRF is the only model that improves the displacement maps for these dates. The WMO stations for each of these cases present good weather conditions (Tab. I: Broken / Overcast). Moreover, one of the cases that remained (20181107-20181113) shows in general a degradation of standard deviations indicating that the troposphere signal was well modeled, but there may be an additional source of error in the displacement maps.

Apart from the correlations with dWV maps, there is no clear relation between an improvement in displacement statistics and the weather conditions. One possible factor can be snow cover. Although, as shown in Fig. 9 the color dots representing the snow appear for different values of correlation and thus, cannot be responsible for a lack of improvement in the displacement studies. The snow cover values vary from $\sim$1.7 cm to $\sim$13.2 cm. For the largest snow cover values, the correlation between the dWV and the improvement is actually the highest for all the models. Thus, for the large snow cover, the correction models may be very helpful. On the other hand, for such weather conditions, the coherence for the interferograms is usually low.

In this study we also check if we can calculate the correction models for smaller areas ($\sim 15 \times 15$ km^2). However, for such scale, most of the models behave similarly, i.e. the semi-variance do not show any differences between the models for the distances below 20 km. As shown in Fig. 7, the size for the areas for which we can implement the correction models should be greater that 20 km. Figure 13 shows the correlation between the semi-variance improvement and the correlation coefficient for dWV. We can see, that the correlation coefficient increases with the distance and at around 30-35 km it reaches a constant level of about $R = 0.52$ for the COMEDIE-WRF and LINEAR models to $R = 0.56$ for the ITD-GNSS model.

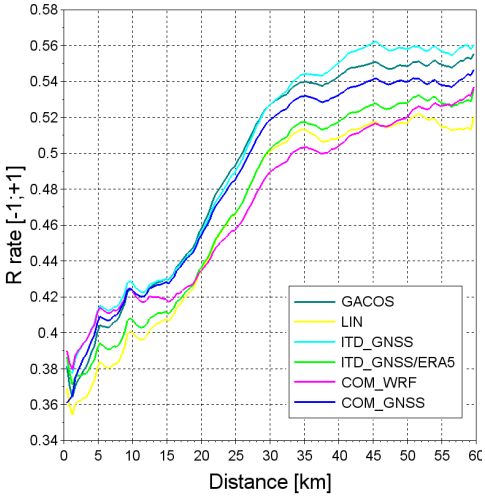

Fig. 13. Correlation between the improvement in semi-variance and R of dWV with respect to the distance.

An important aspect of the discrepancies between different correction models is the fact that they use different types of data: three different weather models and GNSS data (Tab. II). The data sources are sometimes not consistent. A significant bias of 3.8 mm is found between the data for the ERA5

reanalysis model and GNSS data. Similarly, there is a bias between WRF and GNSS which caused the exclusion of many GNSS observations in the COMEDIE-mix models (they were considered as outliers). Due to the bias between data sources, also the ITD-mix model performs worse that the ITD model with only one data source. Thus, the combination of the data sources for our purpose should be done either at an earlier stage of processing (e.g. assimilation of data from GNSS into NWP models [35]) or through new algorithms, taking into account the observed bias [36].

VII. Conclusions

In this study, we presented seven correction models for removing the tropospheric impact on DInSAR estimates for a mining USCB area in Poland. The models were built based on different methods and data sources. The considered models were: GACOS, based on ITD method and HRES model, further ITD models: ITD-GNSS and ITD-mix, combining GNSS and ERA5 data, three COMEDIE-based models with different input sources: COMEDIE-GNSS, COMEDIE-WRF and COMEDIE-mix, and a simple LINEAR model. At first we assessed the models with the reference GNSS data and calculated the similarities between the models based on the correlation coefficients between them. The highest correlation is unsurprisingly between COMEDIE-WRF and COMEDIE-mix, but these two models consist of almost the same data. Very high correlation is also between different models but using the same data sources, i.e. GNSS (COMEDIE-GNSS and ITD-GNSS). Also GACOS and COMEDIE-GNSS are highly correlated, even though they are based on different sources.

The main validation of the proposed models was the application for the DInSAR displacement corrections. For short temporal baselines, there should be no displacement presence, thus, the application of the models should improve the statistics (biases, standard deviations and semi-variograms) for each interferogram. In general, the models that improved mostly the statistics are: GACOS, COMEDIE-WRF, COMEDIE-GNSS and ITD-GNSS. Combined models, so far are not more effective than the ones exploiting one data source. Moreover, the simple linear model only degrade the statistics.

Although, on average, there was a small improvement in the displacement maps after applying our models, some of the interferograms showed a degradation. To determine conditions for which there is a degradation, we calculated a correlations between the water vapor values from SEVIRI radiometer onboard a MSG satellite. We removed the interferograms for which the correlation coefficient was below 0.34. In total, 9 out of the 17 interferograms were removed. The average improvement for the standard deviations and semi-variograms for the remaining interferograms was two times larger than before the removal.

Acknowledgments

This study was made possible by the EPOS project funds under a contract number IODP0000.272.5.2019.EPOS

References

[1] M. Simons and P. Rosen, *Interferometric Synthetic Aperture Radar Geodesy*, 12 2007, vol. 3, pp. 391–446.

[2] C. W. Chen and H. A. Zebker, "Network approaches to two-dimensional phase unwrapping: intractability and two new algorithms," *J. Opt. Soc. Am. A*, vol. 17, no. 3, pp. 401–414, Mar 2000. [Online]. Available: http://josaa.osa.org/abstract.cfm?URI=josaa-17-3-401

[3] T. Nilsson, J. Böhm, D. Wijaya, A. Tresch, V. Nafisi, and H. Schuh, *Path Delays in the Neutral Atmosphere*. Beriln: Springer Atmospheric Sciences, 2013, pp. 193–194.

[4] R. Jolivet, P. S. Agram, N. Y. Lin, M. Simons, M.-P. Doin, G. Peltzer, and Z. Li, "Improving insar geodesy using global atmospheric models," *Journal of Geophysical Research: Solid Earth*, vol. 119, no. 3, pp. 2324–2341, 2014. [Online]. Available: https://agupubs.onlinelibrary.wiley.com/doi/abs/10.1002/2013JB010588

[5] D. Massonnet, K. Feigl, M. Rossi, and F. Adragna, "Radar interferometric mapping of deformation in the year after the landers earthquake," *Nature*, vol. 369, pp. 227–230, 05 1994.

[6] A. Hooper, D. Bekaert, K. Spaans, and M. Arıkan, "Recent advances in sar interferometry time series analysis for measuring crustal deformation," *Tectonophysics*, vol. 514-517, pp. 1 – 13, 2012. [Online]. Available: http://www.sciencedirect.com/science/article/pii/S0040195111004343

[7] Z. W. Li, W. B. Xu, G. C. Feng, J. Hu, C. C. Wang, X. L. Ding, and J. J. Zhu, "Correcting atmospheric effects on insar with meris water vapour data and elevation-dependent interpolation model," *Geophysical Journal International*, vol. 189, no. 2, pp. 898–910, 2012. [Online]. Available: https://onlinelibrary.wiley.com/doi/abs/10.1111/j.1365-246X.2012.05432.x

[8] C. Liang, P. Agram, M. Simons, and E. Fielding, "Ionospheric correction of insar time series analysis of c-band sentinel-1 tops data," 01 2019.

[9] A. Ferretti, C. Prati, and F. Rocca, "Permanent scatterers in sar interferometry," *IEEE Transactions on Geoscience and Remote Sensing*, vol. 39, no. 1, pp. 8–20, Jan 2001.

[10] A. Hooper, P. Segall, and H. Zebker, "Persistent scatterer interferometric synthetic aperture radar for crustal deformation analysis, with application to volcán alcedo, galápagos," *Journal of Geophysical Research: Solid Earth*, vol. 112, no. B7, 2007. [Online]. Available: https://agupubs.onlinelibrary.wiley.com/doi/abs/10.1029/2006JB004763

[11] B. Zhu, J. Li, and W. Tang, "Correcting insar topographically correlated tropospheric delays using a power law model based on era-interim reanalysis," *Remote Sensing*, vol. 9, p. 765, 07 2017.

[12] J. R. Elliott, J. Biggs, B. Parsons, and T. J. Wright, "Insar slip rate determination on the altyn tagh fault, northern tibet, in the presence of topographically correlated atmospheric delays," *Geophysical Research Letters*, vol. 35, no. 12, 2008. [Online]. Available: https://agupubs.onlinelibrary.wiley.com/doi/abs/10.1029/2008GL033659

[13] C. Yu, Z. Li, N. T. Penna, and P. Crippa, "Generic atmospheric correction model for interferometric synthetic aperture radar observations," *Journal of Geophysical Research: Solid Earth*, vol. 123, no. 10, pp. 9202–9222, 2018. [Online]. Available: https://agupubs.onlinelibrary.wiley.com/doi/abs/10.1029/2017JB015305

[14] D. P. S. Bekaert, A. Hooper, and T. J. Wright, "A spatially variable power law tropospheric correction technique for insar data," *Journal of Geophysical Research: Solid Earth*, vol. 120, no. 2, pp. 1345–1356, 2015. [Online]. Available: https://agupubs.onlinelibrary.wiley.com/doi/abs/10.1002/2014JB011558

[15] A. Ferretti, C. Prati, and F. Rocca, "Multibaseline insar dem reconstruction: the wavelet approach," *IEEE Transactions on Geoscience and Remote Sensing*, vol. 37, no. 2, pp. 705–715, March 1999.

[16] Y. Tang, R. Capon, R. Forbes, and P. Clark, "Fog prediction using a very high resolution numerical weather prediction model forced with a single profile," *Meteorological Applications*, vol. 16, pp. 129 – 141, 06 2009.

[17] K. D. Murray, D. P. Bekaert, and R. B. Lohman, "Tropospheric corrections for insar: Statistical assessments and applications to the central united states and mexico," *Remote Sensing of Environment*, vol. 232, p. 111326, 2019. [Online]. Available: http://www.sciencedirect.com/science/article/pii/S0034425719303451

[18] EUMETSAT, "Introduction into the absorption channels," online, accessed 22/11/2019, Nov 2019, http://oiswww.eumetsat.org/WEBOPS/msginterpretation/msgchannels.php.

[19] C. Yu, "System description," online, accessed 22/11/2019, Nov 2019, http://ceg-research.ncl.ac.uk/v2/gacos/.

[20] D. Bekaert, "Toolbox for reducing atmospheric insar noise," online, accessed 22/11/2019, Nov 2019, https://davidbekaert.com/.

[21] C. L. Romain Jolivet, Piyush Agram, "Pyaps documentation," online, accessed 22/11/2019, Nov 2019, http://earthdef.caltech.edu/projects/pyaps/files.
[22] M. Kryza, M. Werner, K. Wałszek, and A. J. Dore, "Application and evaluation of the wrf model for high-resolution forecasting of rainfall–a case study of sw poland," *Meteorologische Zeitschrift*, vol. 22, no. 5, pp. 595–601, 2013.
[23] "Statistics poland," December 2019. [Online]. Available: https://stat.gov.pl/en/
[24] E. Helios-Rybicka, "Environmental impact of the mining industry in poland," *Fuel and Energy Abstracts*, vol. 37, 05 1996.
[25] C. Yu, N. T. Penna, and Z. Li, "Generation of real-time mode high-resolution water vapor fields from gps observations," *Journal of Geophysical Research: Atmospheres*, vol. 122, no. 3, pp. 2008–2025, 2017. [Online]. Available: https://agupubs.onlinelibrary.wiley.com/doi/abs/10.1002/2016JD025753
[26] M. Gospodarki, "Polityka energetyczna polski do 2030 roku," Ministerstwo Gospodarki, Tech. Rep., 2009.
[27] M. Ilieva, A. Borkowski, K. Smolak, and W. Rohm, "Mining deformation life cycle in the light of insar and deformation models," *Remote Sensing*, vol. 11, 03 2019.
[28] B. Mohamadi, T. Balz, and A. Younes, "A model for complex subsidence causality interpretation based on ps-insar cross-heading orbits analysis," *Remote Sensing*, vol. 11, p. 2014, 08 2019.
[29] D. M. A. Aminou, B. Jacquet, and F. Pasternak, "Characteristics of the Meteosat Second Generation (MSG) radiometer/imager: SEVIRI," vol. 3221, pp. 19 – 31, 1997. [Online]. Available: https://doi.org/10.1117/12.298084
[30] K. Sosnica, J. Kaplon, W. Rohm, I. Kudlacik, R. Zajdel, T. Hadas, J. Bosy, J. Sierny, D. Tondas, M. Ilieva, A. Borkowski, J. Krynski, P. Dykowski, G. Mutke, A. Kotyrba, and D. Olszewska, "Monitoring of earth surface displacements using integrated multi-gnss, gravity, seismic, and insar data in the framework of ggos-pl++," 07 2018.
[31] C. Albergel, E. Dutra, S. Munier, J.-C. Calvet, J. Muñoz Sabater, P. Rosnay, and G. Balsamo, "Era-5 and era-interim driven isba land surface model simulations : Which one performs better?" *Hydrology and Earth System Sciences Discussions*, 04 2018.
[32] T. Haiden, M. Janousek, J. Bidlot, R. Buizza, L. Ferranti, F. Prates, and F. Vitart, "Evaluation of ecmwf forecasts, including the 2018 upgrade," 10 2018.
[33] C. Yu, Z. Li, N. T. Penna, and P. Crippa, "Generic atmospheric correction model for interferometric synthetic aperture radar observations," *Journal of Geophysical Research: Solid Earth*, vol. 123, no. 10, pp. 9202–9222, 2018.
[34] K. Wilgan, F. Hurter, A. Geiger, W. Rohm, and J. Bosy, "Tropospheric refractivity and zenith path delays from least-squares collocation of meteorological and gnss data," *Journal of Geodesy*, vol. 91, 08 2016.
[35] E. Trzcina and W. Rohm, "Estimation of 3d wet refractivity by tomography, combining gnss and nwp data: First results from assimilation of wet refractivity into nwp," *Quarterly Journal of the Royal Meteorological Society*, vol. 145, no. 720, pp. 1034–1051, 2019. [Online]. Available: https://rmets.onlinelibrary.wiley.com/doi/abs/10.1002/qj.3475
[36] L. Yang, C. Hill, and T. Moore, "Numerical weather modeling-based slant tropospheric delay estimation and its enhancement by gnss data," *Geo-spatial Information Science*, vol. 16, no. 3, pp. 186–200, 2013. [Online]. Available: https://doi.org/10.1080/10095020.2013.817107